BIOCELL

Tech Science Press

http://doi.org/10.32604/biocell.2026.078925

ARTICLE

Organ-Specific Metabolic Adaptations to Acute Injury and Their Modulation by Fumarate

Marina I. Buyan[1,2,#], Kseniia S. Cherkesova[1,3,#], Anna A. Brezgunova[1], Andrey I. Buyan[4], Polina A. Abramicheva[1], Irina B. Pevzner[1], Nadezda V. Andrianova[1,*] and Egor Y. Plotnikov[1,*]

[1]A. N. Belozersky Institute of Physico-Chemical Biology, Lomonosov Moscow State University, Moscow, Russia
[2]Faculty of Bioengineering and Bioinformatics, Lomonosov Moscow State University, Moscow, Russia
[3]Biological Faculty, Lomonosov Moscow State University, Moscow, Russia
[4]Institute of Protein Research, Russian Academy of Sciences, Pushchino, Russia
*Corresponding Authors: Nadezda V. Andrianova. Email: andrianova@belozersky.msu.ru;
Egor Y. Plotnikov. Email: plotnikov@belozersky.msu.ru
[#]These authors contributed equally to this paper

Received: 10 January 2026; Accepted: 16 March 2026; Published: 29 June 2026

ABSTRACT: Objectives: Metabolic substrate deficiency is a key factor in many pathologies, with organ vulnerability depending on specialized metabolic profiles. In this study, we aimed to investigate the impact of deprivation stress on mitochondria and cell functions in different cell types and to assess the potential of fumarate, a tricarboxylic acid (TCA) cycle intermediate, to modulate these stress responses. **Methods:** We assessed the effects of fumarate on cell proliferation and mitochondrial membrane potential under both normal conditions and serum deprivation *in vitro* in astrocytes, renal epithelial cells, and hepatic stellate cells. Subsequently, we performed bioinformatic analysis of transcriptomic data for brain, kidney, and liver tissues subjected to ischemia to reveal specific patterns of alterations in energy metabolism. **Results:** Analysis of mitochondria-associated gene expression revealed striking organ-specific differences in transcriptional responses to ischemia, with a significant decrease in expression of genes related to the TCA cycle and electron transport chain in the kidneys and liver, in contrast to the brain. In an *in vitro* serum deprivation model, fumarate preserved mitochondrial potential in a cell type-specific manner, with optimal concentrations of 12.5 mM for astrocytes ($p < 0.05$), and 25 mM for renal ($p < 0.01$) or hepatic cells ($p < 0.01$). Under normal conditions, fumarate increased mitochondrial potential in astrocytes ($p < 0.0001$), with weak or no effect on renal and hepatic cells. Estimation of cell number indicates the effects of fumarate on the proliferation of kidney ($p < 0.05$) and liver ($p < 0.0001$) cells in normal conditions and cell death after serum deprivation. **Conclusion:** Bioinformatic analysis demonstrates that ischemic stress induces fundamentally different transcriptional programs in the brain, kidney, and liver, particularly affecting genes involved in mitochondrial bioenergetics. Complementing these findings, our *in vitro* data identify fumarate as a metabolically active but organ-dependent candidate for tissue protective strategies in substrate deprivation pathologies, like ischemia.

KEYWORDS: Brain; kidney; liver; metabolic deprivation; energy substrates; mitochondria; fumarate; tissue-specific metabolism

1 Introduction

Nutrient substrate deficiency and impaired energy metabolism are hallmarks of a wide range of severe pathologies, including cardiovascular diseases, sepsis, and hemorrhagic shock [1,2]. Impaired tissue perfusion often results in ischemia/reperfusion (I/R) injury, characterized by a drastic reduction in oxygen

and energy metabolic substrate delivery due to compromised blood flow [3]. The lack of key energy substrates can be as detrimental as hypoxia itself. Substrate deficiency induces an energetic crisis, disrupts metabolic and biosynthetic processes, and is commonly associated with mitochondrial dysfunction and oxidative stress due to electron transport chain (ETC) impairments. These changes lead to violations in ATP synthesis and failure of ATP-dependent processes and cell homeostasis. Ultimately, metabolic collapse triggers the intrinsic apoptotic pathway or, in cases of severe depletion, leads to necrotic cell death [4].

The kidney, liver, and brain are highly sensitive to disturbances in energy metabolism due to their high and sustained energetic demands. In the brain, astrocytes support the high energy requirements of neurons by supplying lactate as an alternative fuel source via the astrocyte-neuron lactate shuttle [5]. Similarly, renal tubular cells require significant amounts of ATP for the reabsorption of amino acids, glucose, and electrolytes, mediated by ATP-dependent transporters [6]. The liver exhibits high energy expenditure due to its central role in carbohydrate, lipid, and protein metabolism [7]. This metabolic demand is further amplified by the liver's robust regenerative capacity following injury, which requires sustained metabolic activity [8].

One promising approach to correcting energy imbalance involves the use of exogenous intermediates of the tricarboxylic acid (TCA) cycle. Reducing equivalents, produced by the TCA cycle, are essential for ETC function and ATP replenishment. To preserve mitochondrial integrity and function, a continuous flux of reducing equivalents from the TCA cycle to the ETC must be maintained [9]. Among TCA cycle intermediates, fumarate has attracted attention as a metabolite with cytoprotective potential for treating conditions associated with energy substrate deficiency. Under physiological conditions, fumarate, as a product of succinate oxidation and a substrate of fumarate hydratase, serves as an intermediate of the TCA cycle, thereby supporting cellular energy production [10]. Under pathological conditions, the integrity of the cycle is disrupted, and fumarate, losing its role as a mere metabolic intermediate, instead functions as a signaling molecule. Through the activation of Nrf2, it induces the expression of cytoprotective genes, ultimately attenuating oxidative stress and inflammation [11–13]. However, despite increasing interest in fumarate and its derivatives, effective protocols for their use in ischemic pathologies remain insufficiently defined. In particular, the tissue- and cell type-specific effects of fumarate under conditions of metabolic substrate deprivation are poorly understood.

In this study, we aimed to identify organ-specific features of the metabolic responses to ischemic injury and to assess whether exogenous fumarate modulates the viability and mitochondrial function of cells from different organs. To address this, we performed a comparative analysis of transcriptomic data for the brain, kidney, and liver under normal and ischemic conditions, focusing on genes encoding key components of energy metabolism, including proteins of the TCA cycle and ETC. Then, the cellular responses to exogenous fumarate were compared using astrocytes, renal tubular epithelial cells, and hepatic stellate cells under normal and stress conditions *in vitro*. The effects of various fumarate concentrations on cell viability and mitochondrial transmembrane potential were assessed to identify tissue-specific patterns of metabolic sensitivity and adaptation.

2 Materials and Methods

2.1 Bioinformatic Analysis

Differential expression analysis for brain, kidney and liver tissues under basal conditions and after I/R injury was performed using RNA-Seq data from Zhou et al. [14] (for brain, GEO accession number GSE303321), Heruye et al. [15] (for kidney, GSE267650) and microarray data from Zabala et al. [16] (for liver, GSE117915). The former two datasets were analyzed separately using the R (v.4.5.2) package 'edgeR' (v.4.8.0) standard quasi-likelihood pipeline with *filterByExpr* for filtering out lowly expressed genes, *calcNormFactors* for sample

normalization, *estimateDisp*, *glmQLFit* and *glmQLFTest* for fitting the model and testing genes for differential expression [17]. For the liver dataset, probes with maximal median absolute deviation were left for each gene, followed by the standard 'limma' (v.3.66.0) analysis pipeline using *lmFit*, *eBayes* and *topTable* functions. KEGG mmu00190 (Oxidative phosphorylation, https://www.kegg.jp/kegg-bin/show_pathway?mmu00190) and mmu00020 (TCA cycle, https://www.kegg.jp/kegg-bin/show_pathway?mmu00020) pathways [17] colored by mean $\log_2$FC were generated using 'pathview' (v.1.50.0) R package with *kegg.native* = *T*, *same.layer* = *F*, *node.sum* = '*mean*' and *limit* = *list*('*gene*' = *c*(−1, 1), '*cpd*' = 1). Differential expression data for individual genes in the brain, kidneys, and liver are presented in Supplementary Tables S1–S3, respectively. Given differences in experimental models, reperfusion time points, and transcriptomic platforms, inter-organ comparisons were interpreted qualitatively, focusing on the direction and pattern of transcriptional changes rather than direct quantitative equivalence. To test the general enrichment of differentially expressed genes by biological processes, we performed Gene Set Enrichment Analysis (GSEA) with the R package 'fgsea' (v.1.36.0) using $\log_2$FC estimates for gene ranking and Gene Ontology Biological Process (GO BP) gene sets from MSigDB (v.2025.1) [18]. GSEA result visualization was performed in Cytoscape (v.3.10.3) with EnrichmentMap Pipeline Collection (v.1.1.0), which included EnrichmentMap (v.3.5.0), AutoAnnotate (v.1.5.1), WordCloud (v.3.1.4) and clusterMaker2 (v.2.3.4).

2.2 Cell Cultures

Cultures of kidney epithelial cells NRK-52E (CL-0174, SYNTHBIO, Hefei, China), hepatic stellate cells LX-2 (CL-0560, SYNTHBIO, Hefei, China), and a primary culture of astrocytes obtained from neonatal rats were used. NRK-52E and LX-2 cell lines were cultured in medium supplemented with 10% FBS (HiMedia, Maharashtra, India) and 1% l-glutamine. All cell lines were cultured at 37°C in an atmosphere containing 5% CO_2. All cell cultures used in this study tested negative for mycoplasma contamination and were certified by short tandem repeat (STR) profiling.

Primary cell culture of astrocytes was obtained from the cerebral cortex of 1–2-day-old male Wistar rats (n = 6) [19]. Randomization and blinding were applied during animal allocation. All animal procedures were carried out in accordance with the guidelines of the Federation of European Scientific Associations for Laboratory Animal Use and the ARRIVE guidelines [20]. Animal protocols were approved by the Ethics Committee of the A. N. Belozersky Institute of Physico-Chemical Biology, Lomonosov Moscow State University (Protocol 019-4/07/2025). For the experiments, neonatal rats were humanely euthanized with CO_2. The brain was aseptically removed, and the cortex was dissected. After careful removal of the meninges, the cortical tissue was cut into small pieces and incubated in 0.05% trypsin-EDTA (BioinnLabs, Rostov-on-Don, Russia) solution for 30 min at 37°C. After enzymatic dissociation, the tissue was washed twice with Dulbecco's phosphate-buffered saline (DPBS: Na_2HPO_4 8 mM, NaCl 137.4 mM, KH_2PO_4 1.47 mM, KCl 2.7 mM, $CaCl_2$ 0.9 mM, $MgCl_2$ 0.5 mM, pH 7.4) and resuspended in a complete culture medium consisting of a 1:1 mixture of DMEM with 1 g/L glucose (BioinnLabs, Rostov-on-Don, Russia) and F-12, supplemented with 1% L-glutamine and 10% FBS (HiMedia, Maharashtra, India). The resulting cell suspension was seeded into culture flasks pre-coated with 10 μg/mL poly-D-lysine (Sigma Aldrich, St. Louis, MO, USA) and was maintained at 37°C in an atmosphere of 5% CO_2. On 5–6 days of cultivation, the flasks were shaken at 37°C for 16 h at 200 rpm to remove microglial cells and obtain an enriched astrocyte culture.

To investigate the effect of fumarate (D830225, Macklin, Shanghai, China), all three cell types were seeded into 96-well plates at a density of 5000 cells per well. Upon reaching 50% confluency, the medium in the control wells was replaced with fresh complete growth medium. For the experimental groups, cells were treated with medium containing fumarate dissolved in culture medium at concentrations ranging from

12.5 to 100 mM, potential osmotic or ionic contributions were taken into account as a general limitation of high-millimolar treatments. Serum deprivation was performed by incubating cells in a medium containing all standard components except FBS. Cells were subjected to serum-deprived conditions and/or fumarate treatment for 48 h, after which they were processed for further analysis. For all treatment conditions, the pH of the medium was routinely monitored to ensure the absence of gross pH shifts using phenol red as an indicator.

2.3 Western Blotting

For Western blotting, primary astrocytes, LX-2, and NRK-52E cells were seeded in T-25 cell culture flasks and cultured under normal conditions or subjected to serum deprivation for 48 h. After incubation, cells were washed from the medium and lysed with ice-cold RIPA buffer (Merck Millipore, Darmstadt, Germany) containing 1 mM protease inhibitor phenylmethylsulfonyl fluoride (Helicon, Moscow, Russia) and 1 mM phosphatase inhibitor sodium orthovanadate (Sigma–Aldrich, St. Louis, MO, USA). The lysates were centrifuged at 3000× *g* for 3 min, the supernatants were mixed with 4× sample buffer containing 10% 2-mercaptoethanol and boiled for 5 min. The total protein concentration in the samples was measured using a bicinchoninic acid assay (Sigma-Aldrich, St. Louis, MO, USA). Cell samples (10 μg protein/lane) were loaded onto 10%–20% Tris-glycine polyacrylamide gels. After electrophoresis, gels were transferred onto PVDF membranes (Amersham Pharmacia Biotech, Amersham, UK). Membranes were blocked with 5% non-fat milk in PBS with 0.1% Tween-20 and then incubated with primary antibodies: anti-Complex IV subunit IV 1:1000 mouse (A21348, Invitrogen, Thermo Fisher Scientific, Waltham, MA, USA) and anti-glyceraldehyde 3-phosphate dehydrogenase (GAPDH) 1:1000 rabbit (5G4cc, HiTest, Moscow, Russia). Membranes were then incubated with secondary antibodies, anti-rabbit IgG or anti-mouse IgG conjugated with horseradish peroxidase 1:5000 (IMTEK, Moscow, Russia), and probed with Advansta Western Bright ECL kit (Advansta, San Jose, CA, USA). Detection was performed by a ChemiDoc Imaging System (BioRad, Hercules, CA, USA), density of bands was quantified using ImageJ software.

2.4 Cell Number Assessment

To evaluate the effect of fumarate on cell number under normal and serum-deprived conditions, a 4′,6-diamidino-2-phenylindole (DAPI, Lumiprobe, Moscow, Russia) staining assay was performed, which enabled assessment of proliferation or cytotoxic effects. Following the 48-h incubation in either complete or serum-free medium with or without fumarate at concentrations of 12.5, 25, 50, and 100 mM, all three cell types were washed once with phosphate-buffered saline (PBS, 0.01 M, pH 7.4) and then fixed with 4% formaldehyde solution in PBS for 15 min at room temperature. After fixation, the cells were washed three times with PBS containing 0.02% sodium azide (Helicon, Moscow, Russia) to remove the fixative. Cell nuclei were stained with DAPI (300 nM in PBS) for 30 min at room temperature, protected from light. Following three final washes with PBS, the samples were kept in PBS for imaging. Fluorescence images were acquired using a CELENA® X High Content digital imaging system (Logos Biosystems, Anyang-si, Gyeonggi-do, Republic of Korea) with fluorescence filter cube DAPI (Ex 375/28, Em 460/50). We performed 10 replicates for each experimental group. Quantitative image analysis was performed using CELENA® X Cell Analyzer software (Logos Biosystems, Anyang-si, Gyeonggi-do, Republic of Korea).

2.5 Mitochondrial Transmembrane Potential Assessment

To assess changes in mitochondrial membrane potential, all cell cultures were incubated with 12.5–100 mM disodium fumarate (referred to as fumarate) (Macklin, Shanghai, China) for 48 h under normal

or serum-deprived conditions and stained with 200 nM tetramethylrhodamine ethyl ester (T669, TMRE, Invitrogen, Carlsbad, CA, USA) for 20 min at 37°C. TMRE-loaded cells were visualized using a ZEISS LSM 900 microscope (Carl Zeiss AG, Oberkochen, Germany) with fluorescence settings (Ex 543, Em 616–700). We performed 10 replicates for each experimental group. Average TMRE fluorescence intensity was assessed using Fiji/ImageJ software (version 1.8.0/1.54p, Bethesda, MD, USA).

2.6 Viability Assessment

Cell viability was assessed using the methylthiazolyl tetrazolium (MTT) assay (Macklin, Shanghai, China). The reagent was diluted to a concentration of 5 g/L in DMEM/F-12 medium without sodium bicarbonate (GE Healthcare, Chicago, IL, USA), and incubation was carried out for 1 h at 37°C. Subsequently, cells were lysed with dimethyl sulfoxide (DMSO, Macklin, Shanghai, China), and optical density was measured at a wavelength of 595 nm using a Zenyth 3100 multimodal plate reader (Anthos Labtec, Salzburg, Austria). Wells containing cells incubated in water for 48 h served as negative controls. We performed 10 replicates for each experimental group.

2.7 Statistical Analysis

The statistical data analysis was performed using the GraphPad Prism 9 software (version 9.5.1, San Diego, CA, USA). All values are presented as mean ± standard error of the mean. The data were tested for normal distribution using the Shapiro–Wilk test. Data were analyzed using one-way analysis of variance (ANOVA) with Tukey's multiple comparison test or Kruskal–Wallis test with Dunn's multiple comparison test for normally and non-normally distributed data, respectively. Outliers were removed from the analysis using the ROUT method (Q = 1%). Differences were considered statistically significant at $p < 0.05$.

3 Results

3.1 Transcriptome Analysis of Brain, Kidney, and Liver Following I/R

I/R, resulting from a temporary cessation of blood flow and its subsequent restoration, leads to an acute deficiency of energy substrates in tissues. This condition triggers a cascade of metabolic disturbances, the central component of which is mitochondrial dysfunction and disruption of energy production [21]. Since different organs possess varying degrees of metabolic plasticity, the changes in energy metabolism can be highly organ-specific [22]. In this study, we analyzed the transcriptomic responses of the brain, kidneys and liver to ischemic injury, focusing on the expression of genes encoding key components of ETC and the TCA cycle, to assess the adaptive potential of energy metabolism across different tissues.

Our analysis demonstrated that I/R injury induced transcriptional changes in a broad set of genes in a tissue-specific manner (Fig. 1a–c, Supplementary Figs. S1–S3). Particularly, we detected 2332 downregulated and 2922 upregulated genes out of 17,459 expressed in the brain, 3344 and 3845 out of 15,793 in the kidney, and 698 and 1173 out of 22,340 in the liver, respectively. To compare more deeply the differences in these organs, we performed additional GSEA analysis and showed that in each organ, genes involved in the induction of the inflammatory response were highly upregulated under I/R, as well as the processes of stress response and apoptosis (Supplementary Figs. S1–S3). Simultaneously, a large number of pathways whose regulation was altered by I/R were related to energy metabolism and mitochondrial function. Notably, genes involved in metabolic regulation were downregulated in the kidney and liver, while being upregulated in the brain (Supplementary Figs. S1–S3).

Due to the major role of energy crisis in the pathogenesis of I/R, we assessed in greater detail the changes in gene expression of proteins involved in energy metabolism. We discovered that the pattern

of these changes was specific to each organ (Figs. 2–4). In the brain following I/R, the expression of ETC and TCA cycle genes exhibited an upward trend rather than a decline (Fig. 2). In particular, the expression of TCA genes (*Idh1*, *Pck2*) and subunits of Complex I, Complex III, Complex IV increased, while at the same time a decrease in the expression of *Fh1*, which converts fumarate to malate, was observed. These results suggest a more robust compensatory response to energy deficit in the brain tissue. Conversely, the kidney exhibited a marked downregulation of genes involved in TCA cycle (*Pcx*, *Cs*, *Aco1*, *Idh1*, *Ogdh*, *Dist*, *Sucla2*, *Sdhc*, *Fh1*, etc.) and all complexes of ETC (Fig. 3), suggesting suppressed energy metabolism following I/R. In the liver, a more moderate decrease in the expression of TCA cycle (*Acly*, *Idh1*, etc.) and ETC (Complex III) genes was observed (Fig. 4), similarly indicating transcriptional downregulation of energy metabolic pathways as a consequence of ischemia. Furthermore, transcriptomic analysis revealed increased expression of the transmembrane fumarate receptor *Hcar2* and the transporter *Slc13a3* in brain tissue following ischemic injury (Supplementary Table S1). In contrast, renal tissue exhibited upregulated *Hcar2* expression alongside downregulated *Slc13a3* (Supplementary Table S2), while hepatic tissue showed minimal changes in either gene. These findings indicate that ischemic injury induces organ-specific dysregulation of oxidative phosphorylation pathways, particularly those associated with fumarate metabolism. This tissue-specific metabolic remodeling identifies fumarate-related pathways as potential therapeutic targets for mitigating ischemic damage.

To further link the transcriptomic observations with the *in vitro* injury model, we performed Western blot analysis of representative bioenergetic markers in the three cell lines used in this study (Supplementary Fig. S4). In astrocytes, serum deprivation was associated with an increase in the level of Complex IV subunit IV, while no significant change was observed in kidney epithelial or hepatic stellate cells. In contrast, kidney epithelial cells showed increased GAPDH levels under deprivation conditions, suggesting a potential shift toward glycolytic metabolism.

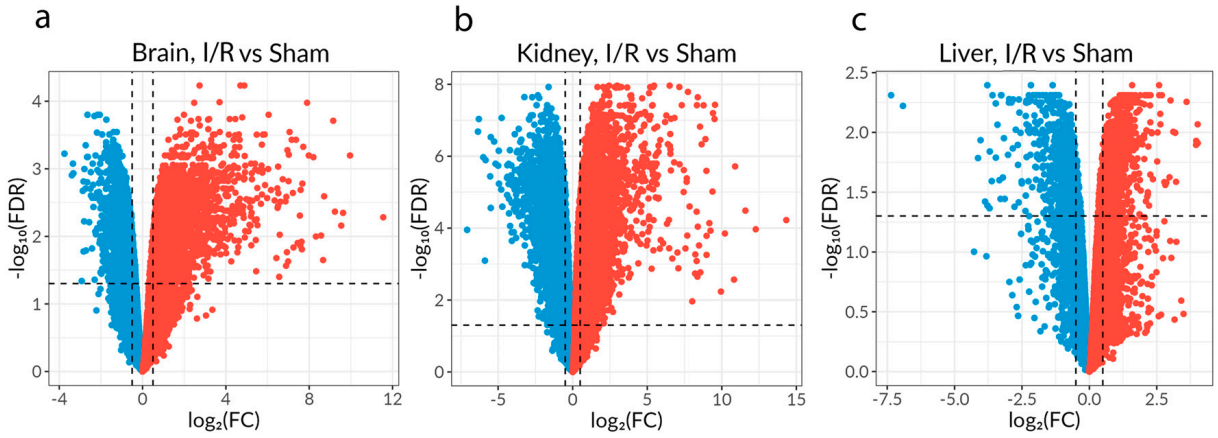

Figure 1: Differential gene expression analysis results in the tissues after I/R injury. (**a**) The number of up- and downregulated genes in the brain after ischemic stroke. (**b**) The amount of up- and downregulated genes in the kidney after renal I/R. (**c**) The amount of up- and downregulated genes in the liver after hepatic I/R. *X*-axis: $\log_2$(Fold Change). *Y*-axis: $-\log_{10}$(False Discovery Rate). Dashed vertical lines indicate $|\log_2(\text{Fold Change})| = 0.5$, horizontal line indicates FDR = 0.05. FC, fold change; FDR, false discovery rate; I/R, ischemia/reperfusion injury. Red dots indicate the genes upregulated after I/R, and blue dots represent downregulated genes.

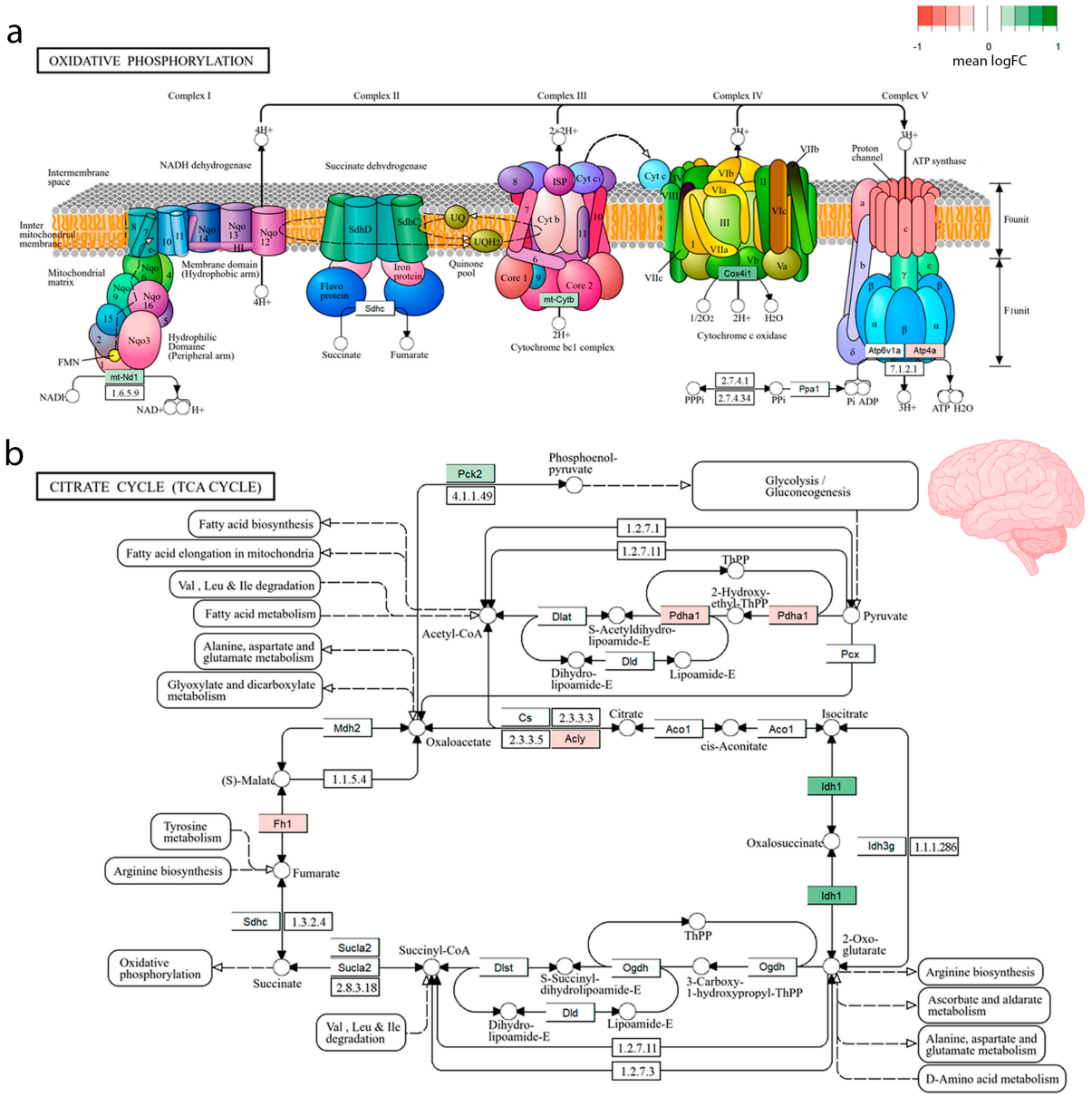

Figure 2: Visualization of gene expression changes in key mitochondrial metabolic pathways following brain I/R. KEGG [17] pathway maps for oxidative phosphorylation ((**a**), adapted from https://www.kegg.jp/kegg-bin/show_pathway?mmu00190) and the TCA cycle ((**b**), adapted from https://www.kegg.jp/kegg-bin/show_pathway?mmu00020) are overlaid with transcriptomic data from brain tissue (corresponding to Fig. 1a). Enzyme boxes color indicates the mean $\log_2$ fold change for genes associated with each reaction step, providing a spatial overview of transcriptional alterations, from downregulation (red shades) to upregulation (green shades) after I/R. Color gradient denotes mean $\log_2$ fold change from differential gene expression analysis of I/R samples versus control.

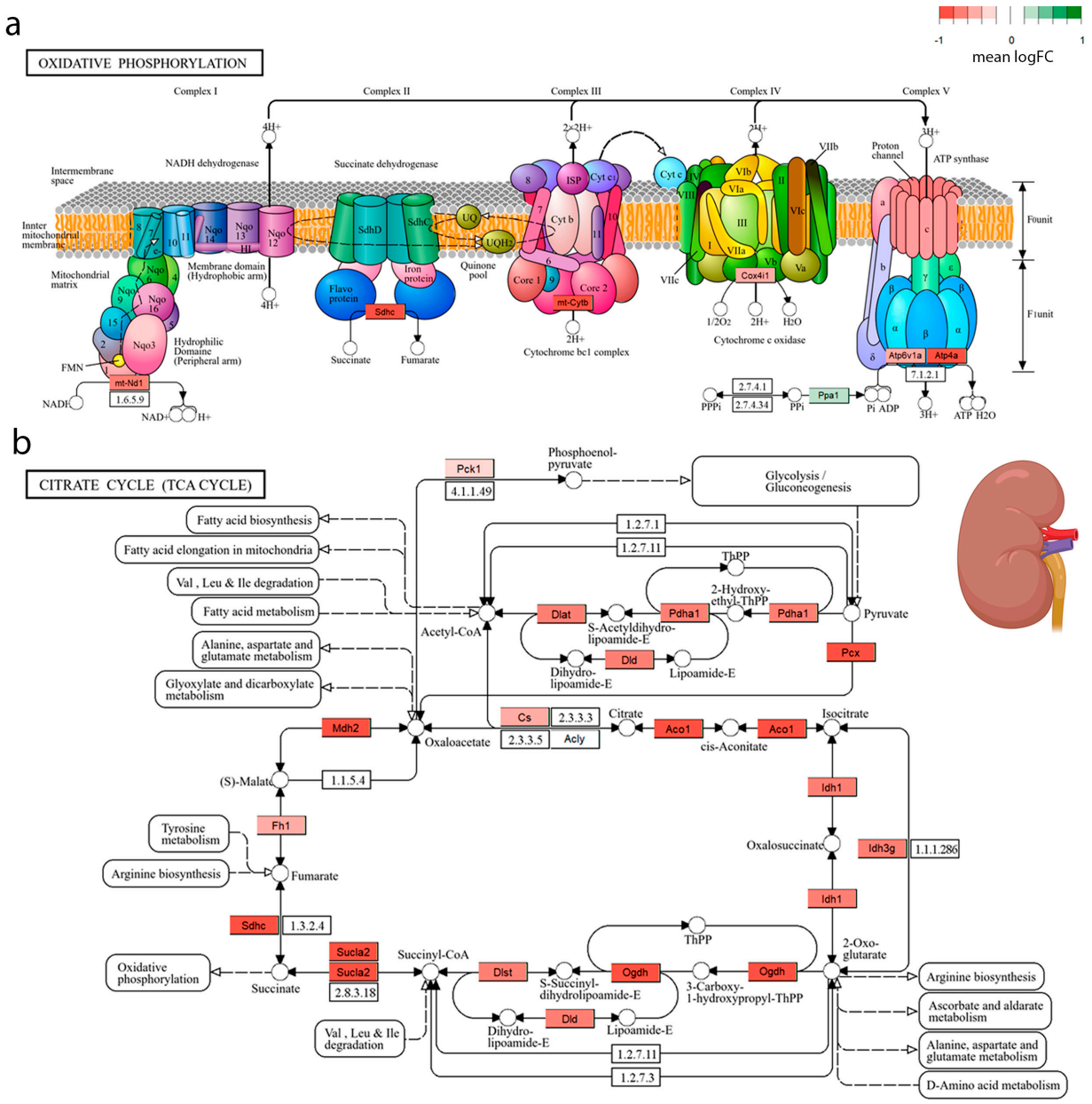

Figure 3: Visualization of gene expression changes in key mitochondrial metabolic pathways following kidney I/R. KEGG [17] pathway maps for oxidative phosphorylation ((**a**), adapted from https://www.kegg.jp/kegg-bin/show_pathway?mmu00190) and the TCA cycle ((**b**), adapted from https://www.kegg.jp/kegg-bin/show_pathway?mmu00020) are overlaid with transcriptomic data from kidney tissue (corresponding to Fig. 1b). Enzyme boxes color indicates the mean $\log_2$ fold change for genes associated with each reaction step, providing a spatial overview of transcriptional alterations with downregulation (red shades) after I/R. Color gradient denotes mean $\log_2$ fold change from differential gene expression analysis of I/R samples versus control.

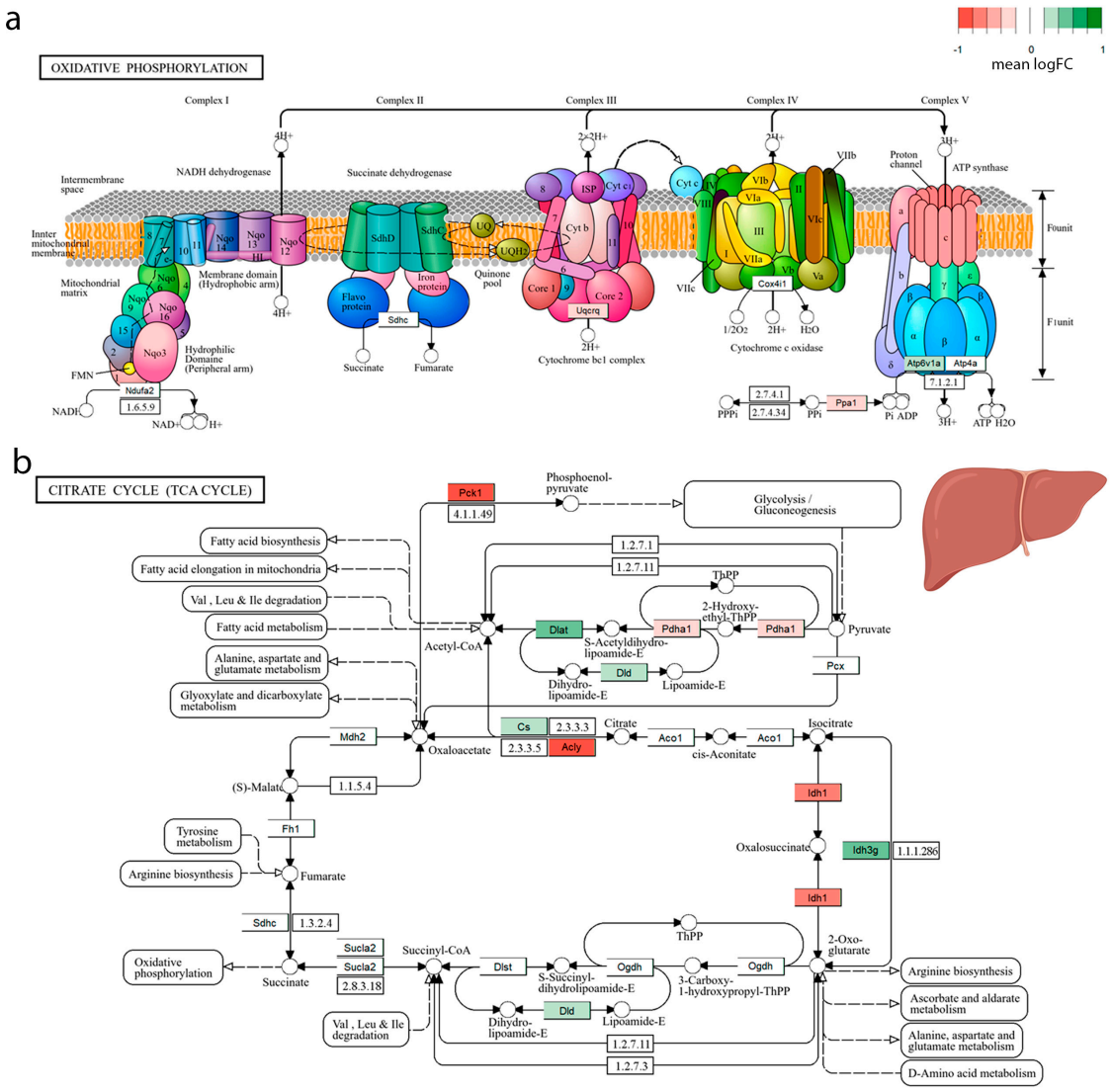

Figure 4: Visualization of gene expression changes in key mitochondrial metabolic pathways following liver I/R. KEGG [17] pathway maps for oxidative phosphorylation ((**a**), adapted from https://www.kegg.jp/kegg-bin/show_pathway?mmu00190) and the TCA cycle ((**b**), adapted from https://www.kegg.jp/kegg-bin/show_pathway?mmu00020) are overlaid with transcriptomic data from liver tissue (corresponding to Fig. 1c). Enzyme boxes color indicates the mean $\log_2$ fold change for genes associated with each reaction step, providing a spatial overview of transcriptional alterations from downregulation (red shades) to upregulation (green shades) after I/R. Color gradient denotes mean $\log_2$ fold change from differential gene expression analysis of I/R samples versus control.

3.2 Effect of Fumarate on the Cell Number and Viability of Astrocytes, Kidney Epithelial Cells, and Hepatic Stellate Cells under Normal and Serum-Deprived Conditions

Cell count after a 48-h fumarate incubation revealed its cell type-specific effects under both normal and serum-deprived conditions (Figs. 5–7).

In the astrocyte culture, all tested concentrations of fumarate (12.5, 25, 50 and 100 mM) in normal medium reduced cell number compared to the control (Fig. 7a). Conversely, under the same conditions some fumarate concentrations promoted proliferation of kidney epithelial cells (at 25 and 50 mM) and hepatic stellate cells (at 25 mM) (Fig. 7b,c). Notably, the highest concentration of fumarate (100 mM) was

particularly toxic to both kidney epithelial and hepatic stellate cells under normal conditions, causing a marked reduction in cell count (Fig. 7b,c).

Serum deprivation significantly reduced cell count in all cell lines compared to the normal-condition control (Fig. 7d–f), suggesting increased cell death. In astrocyte cultures, high concentrations of fumarate (50 and 100 mM) significantly increased cell number compared to the untreated deprivation group (Fig. 7d), indicating some cytoprotective effect. In kidney epithelial cells under stress conditions, incubation with all tested fumarate concentrations resulted in an even greater reduction in cell number (Fig. 7e). Hepatic stellate cells under serum-deprived conditions generally did not show a significant response to fumarate treatment in terms of cell count, although exposure to 100 mM fumarate resulted in a further reduction in cell viability (Fig. 7f).

Assessment of cell metabolic activity using the MTT assay further highlighted cell type-specific effects of fumarate, which in some cases differed from the changes in cell count (Fig. S5).

In astrocyte cultures under normal conditions, fumarate incubation resulted in a marked increase in metabolic activity across the entire concentration range of 12.5 to 100 mM, with the most pronounced effect observed at 50 mM (Fig. S5a). Under serum-deprived conditions, fumarate also exerted a protective effect on astrocytes. Concentrations of 12.5, 50, and 100 mM significantly increased cell viability compared to the untreated deprivation group, with the maximum effect again achieved at 50 mM fumarate (Fig. S5d).

The response of kidney epithelial cells to fumarate was highly dependent on culture conditions. In normal conditions, fumarate exhibited cytotoxic effects, reducing cell viability, particularly at high concentrations of 50 and 100 mM (Fig. S5b). However, under serum-deprived conditions, fumarate at concentrations of 12.5, 25, and 50 mM significantly enhanced the viability of kidney epithelial cells compared to the stressed control (Fig. S5e). Notably, the concentration of 100 mM remained toxic regardless of incubation conditions (Fig. S5e).

In hepatic stellate cells, the effect of fumarate on metabolic activity was more moderate. A slight increase in viability under normal conditions was observed only at 25 mM fumarate (Fig. S5c). Under deprivation conditions, hepatic stellate cell viability remained unaffected by fumarate treatment at concentrations of 12.5–50 mM (Fig. S5f). The concentration of 100 mM, as in kidney epithelial cells, exerted a toxic effect both under normal conditions and during serum deprivation (Fig. S5c,f).

3.3 Effects of Fumarate on the Mitochondrial Transmembrane Potential of Astrocytes, Renal Epithelial Cells and Hepatic Stellate Cells

Mitochondrial functions were assessed by measuring changes in the mitochondrial transmembrane potential ($\Delta\Psi m$) in astrocytes, renal epithelial cells and hepatic stellate cells (Figs. 8–10) by loading with $\Delta\Psi m$-sensitive probe TMRE. A 48-h fumarate treatment significantly increased TMRE fluorescence intensity of astrocytes under normal conditions at concentrations of 12.5, 25, and 50 mM (Fig. 10a). In kidney epithelial cells, only incubation with 25 mM fumarate effectively enhanced TMRE accumulation (Fig. 10b). However, fumarate treatment did not influence the mitochondrial transmembrane potential in hepatic stellate cells at concentrations of 12.5–50 mM, but a significant reduction was observed at 100 mM (Fig. 10c).

A 48-h serum deprivation induced a decrease in $\Delta\Psi m$ across all investigated cell types (Fig. 10d–f) as indicated by a sharp and significant drop in TMRE fluorescence intensity. Fumarate treatment mitigated the drop in $\Delta\Psi m$, although the effective concentrations differed for the specific cell type. The maximum effect on TMRE accumulation in astrocytes was observed for 12.5 mM fumarate (Fig. 10d), whereas in kidney epithelial cells and hepatic stellate cells, the highest effect was observed at 25 mM (Fig. 10e,f).

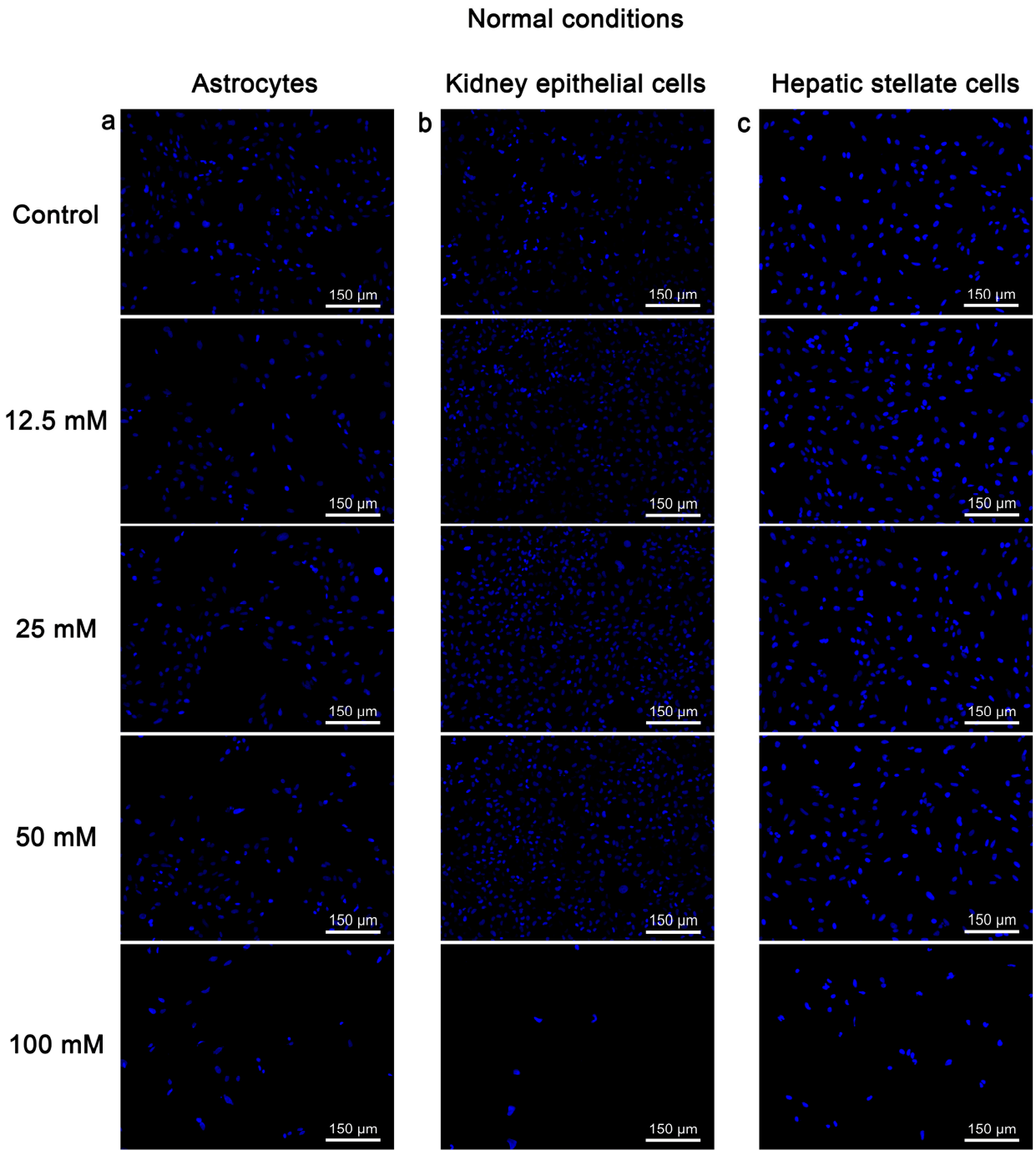

Figure 5: Representative fluorescent images of various cell types stained with DAPI after a 48-h incubation with different concentrations of fumarate (indicated on the left) under normal conditions. (**a**) The number of astrocytes after incubation with fumarate. (**b**) The number of kidney epithelial cells after incubation with fumarate. (**c**) The number of hepatic stellate cells after incubation with fumarate. Scale bar, 150 µm.

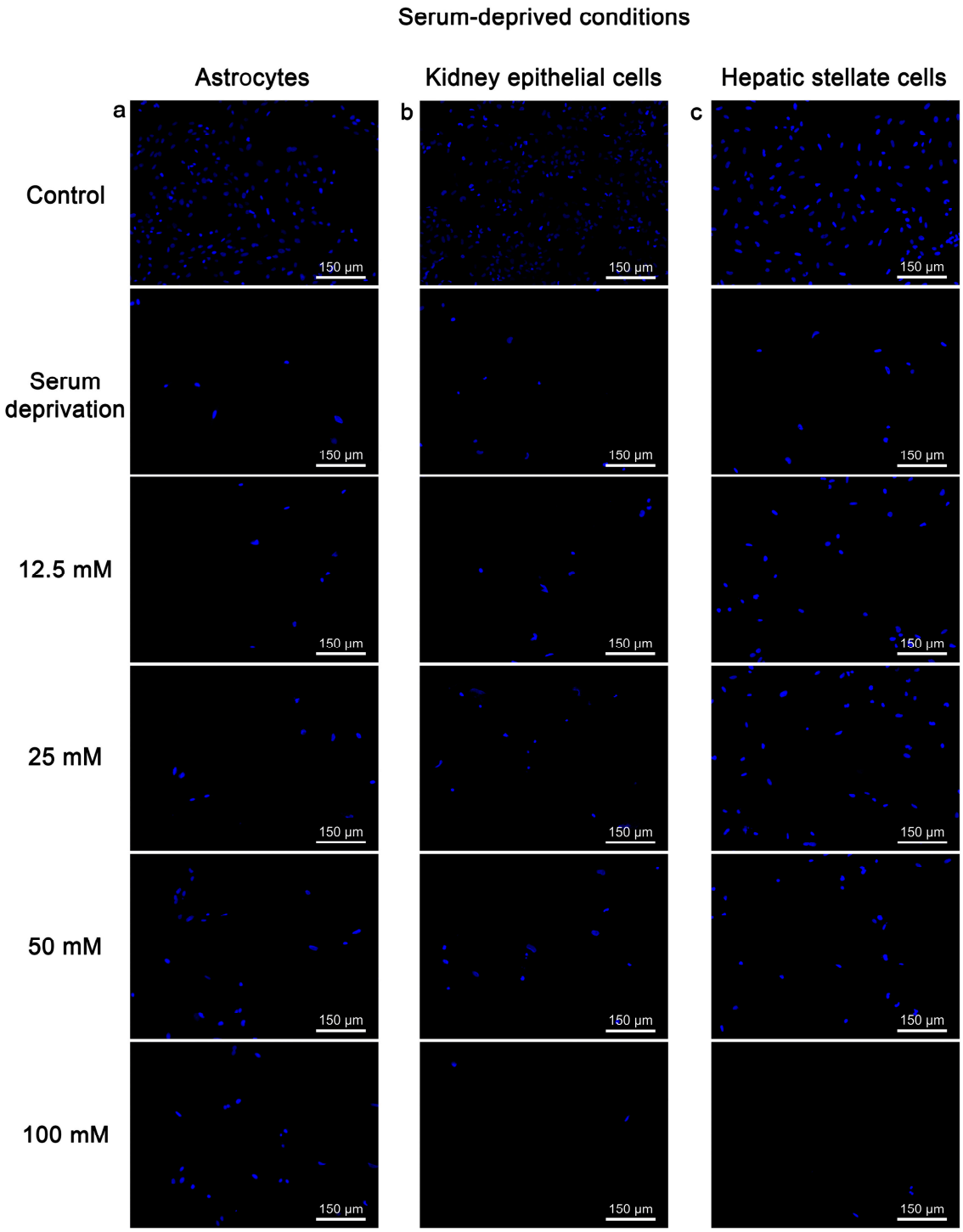

Figure 6: Representative fluorescent images of various cell types stained with DAPI following a 48-h incubation with different concentrations of fumarate (indicated on the left) under serum-deprived conditions. (**a**) The number of astrocytes after serum deprivation with or without fumarate treatment. (**b**) The number of kidney epithelial cells after serum deprivation with or without fumarate treatment. (**c**) The number of hepatic stellate cells after serum deprivation with or without fumarate treatment. Scale bar, 150 µm.

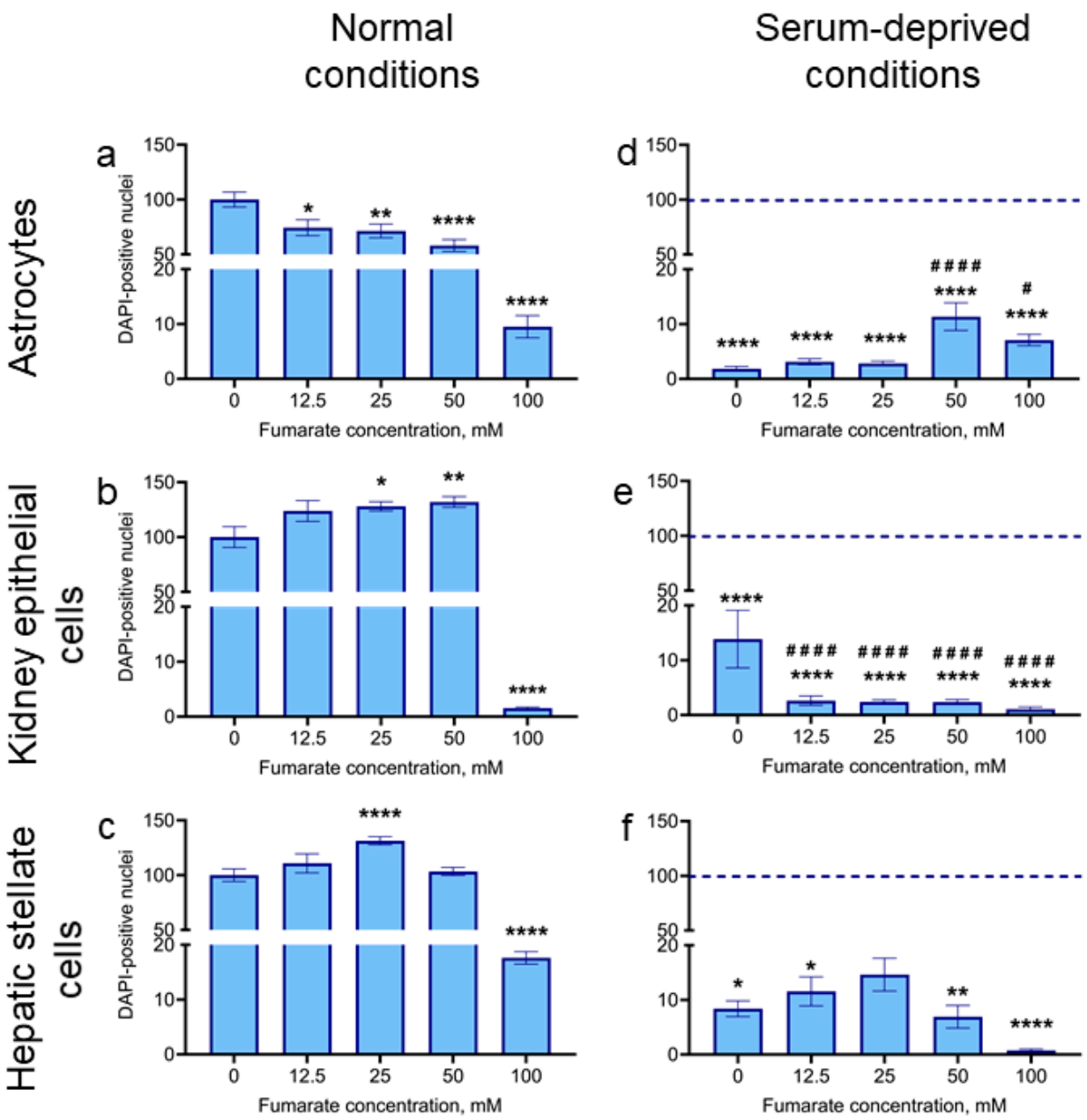

Figure 7: The effect of fumarate on the cell count of astrocytes, kidney epithelial cells, and hepatic stellate cells under normal and serum-deprived conditions. The number of astrocytes (**a**,**d**), kidney epithelial cells (**b**,**e**), and hepatic stellate cells (**c**,**f**) under normal (**a**–**c**) or serum-deprived (**d**–**f**) conditions was assessed by DAPI staining after 48 h of incubation with appropriate media. Data presented as mean ± SEM. One-way ANOVA with post-hoc Tukey's multiple comparisons test; $^{*}p < 0.05$, $^{**}p < 0.01$, $^{****}p < 0.0001$ relative to the control group under normal conditions without fumarate; $^{\#}p < 0.05$, $^{\#\#\#\#}p < 0.0001$ relative to the control group under serum-deprived conditions without fumarate.

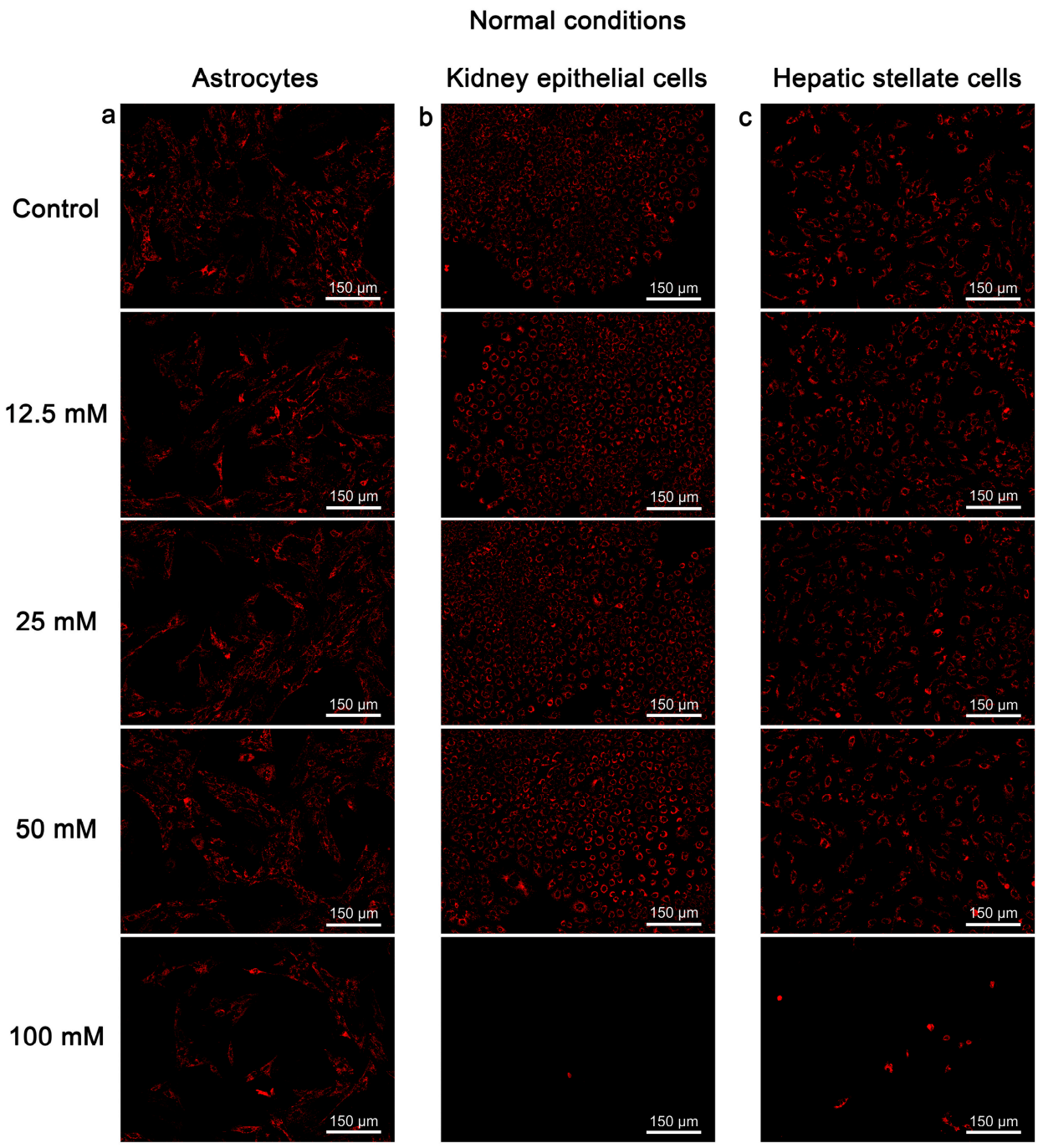

Figure 8: Representative fluorescent images of TMRE-loaded cells after a 48-h incubation with different concentrations of fumarate (indicated on the left) under normal conditions. (**a**) Evaluation of mitochondrial transmembrane potential of astrocytes after incubation with fumarate. (**b**) Evaluation of mitochondrial transmembrane potential of kidney epithelial cells after incubation with fumarate. (**c**) Evaluation of mitochondrial transmembrane potential of hepatic stellate cells after incubation with fumarate. Scale bar, 150 µm.

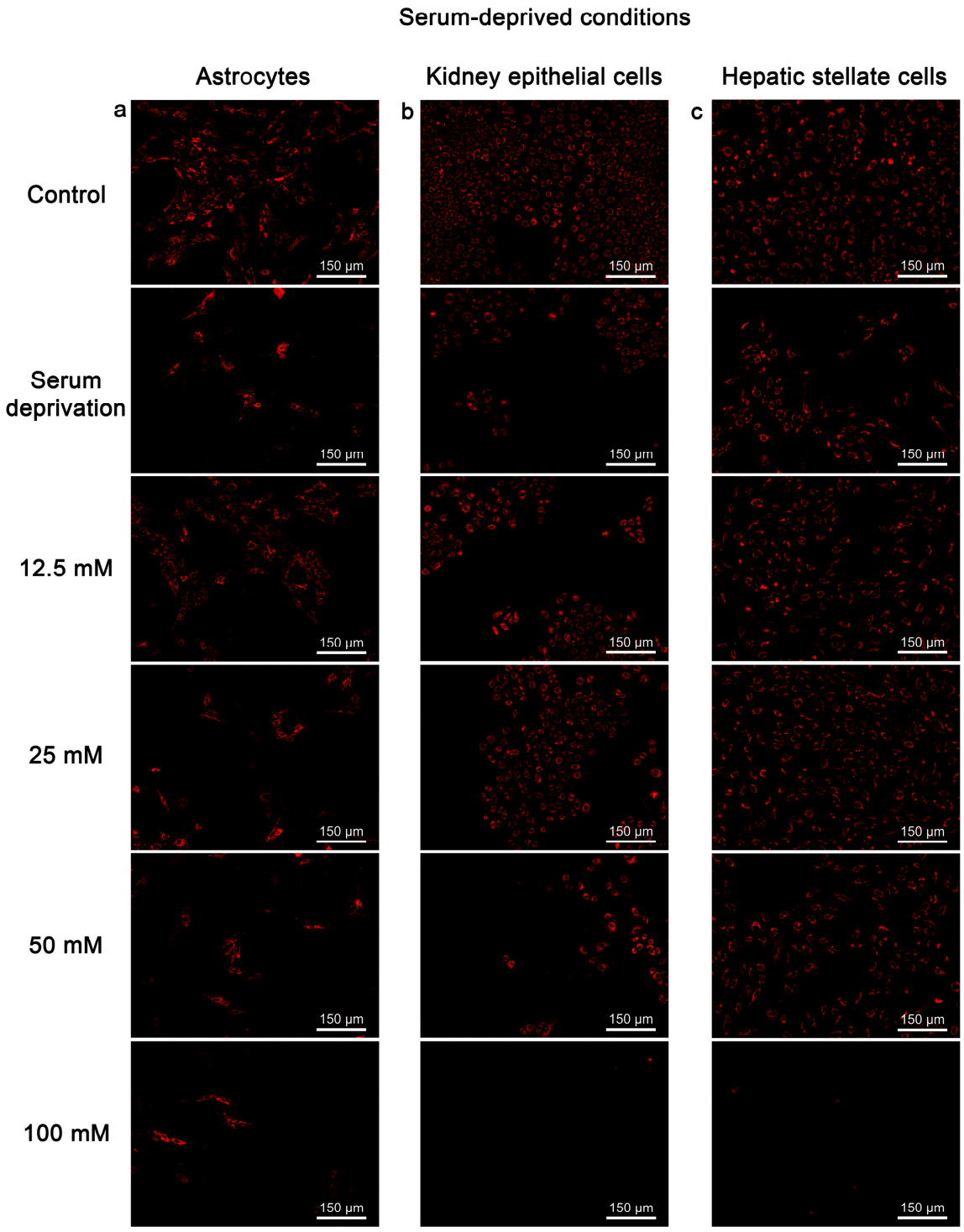

Figure 9: Representative fluorescent images of TMRE-loaded cells after a 48-h incubation with different concentrations of fumarate (indicated on the left) under serum-deprived conditions. (**a**) Evaluation of mitochondrial transmembrane potential of astrocytes after serum deprivation with or without fumarate treatment. (**b**) Evaluation of mitochondrial transmembrane potential of kidney epithelial cells after serum deprivation with or without fumarate treatment. (**c**) Evaluation of mitochondrial transmembrane potential of hepatic stellate cells after serum deprivation with or without fumarate treatment. Scale bar, 150 µm.

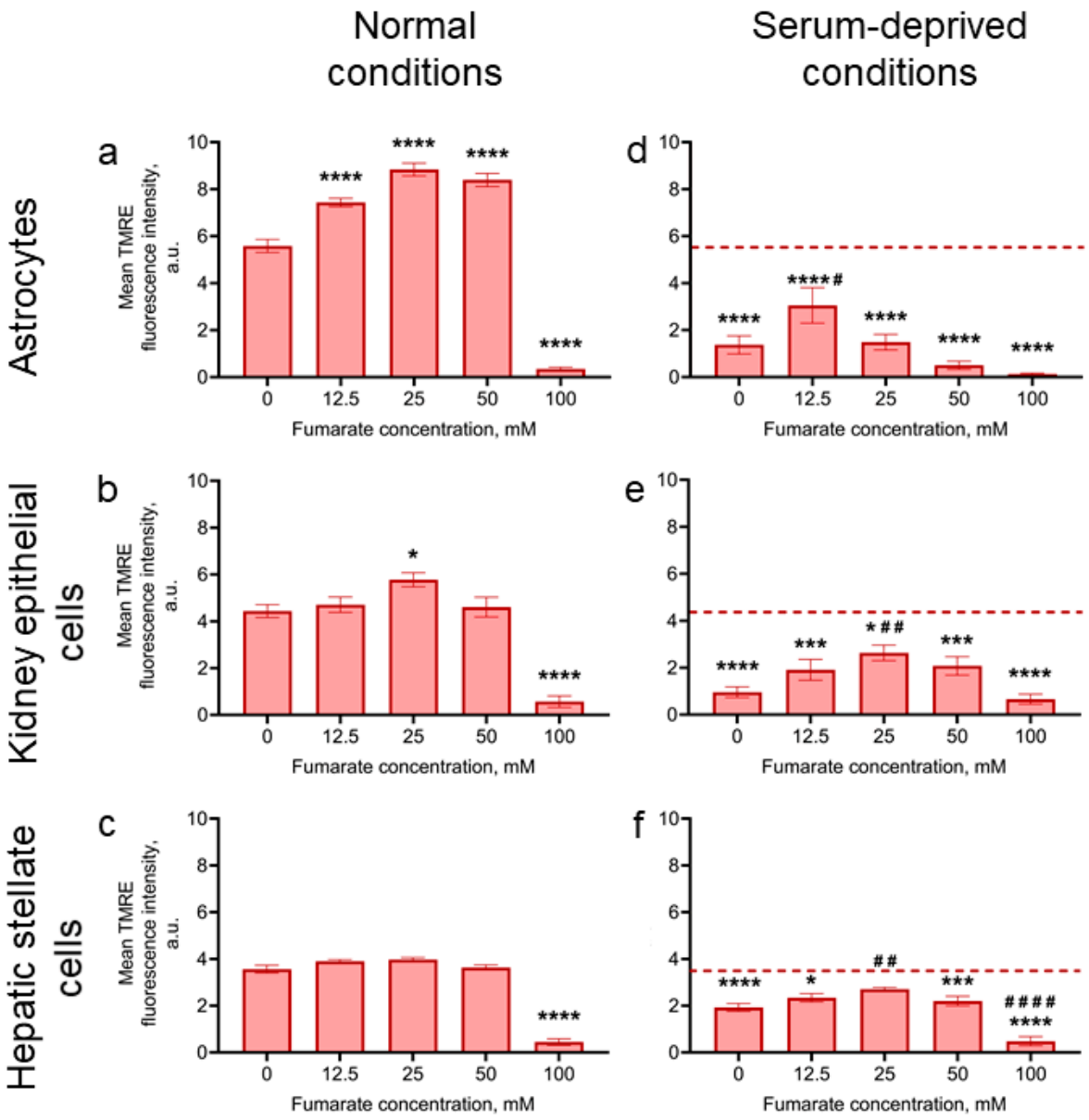

Figure 10: Changes in the mitochondrial transmembrane potential-associated TMRE signal in astrocytes, kidney epithelial cells, and hepatic stellate cells upon incubation with different concentrations of fumarate under normal and serum-deprived conditions. Mean TMRE fluorescence intensity in astrocytes (**a**,**d**), kidney epithelial cells (**b**,**e**), and hepatic stellate cells (**c**,**f**) under normal (**a**–**c**) or serum-deprived (**d**–**f**) conditions. Data presented as mean ± SEM. One-way ANOVA with post-hoc Tukey's multiple comparisons test; $^{*}p < 0.05$, $^{***}p < 0.001$, $^{****}p < 0.0001$ relative to the control group under normal conditions without fumarate; $^{\#}p < 0.05$, $^{\#\#}p < 0.01$, $^{\#\#\#\#}p < 0.0001$ relative to the control group under serum-deprived conditions without fumarate.

4 Discussion

The deficiency of energy substrates is a central pathophysiological mechanism underlying many acute and chronic ischemic conditions. This deficit arises primarily as a consequence of impaired tissue perfusion, which limits the delivery of oxygen and metabolic substrates. One of the most common causes of such substrate deprivation is I/R injury [23]. I/R injury may develop locally due to vascular or circulatory

impairments, as in myocardial infarction, stroke, or kidney and liver ischemia. It can also occur at a systemic level during shock caused by massive hemorrhage or severe trauma [24]. In these conditions, sudden intravascular volume loss triggers reduced tissue perfusion, impaired oxygen and nutrient delivery, and ultimately, the development of multiple organ failure [25].

Impaired blood supply is often associated with alterations in mitochondrial homeostasis. A deficit of metabolic substrates and oxygen suppresses mitochondrial function and may be accompanied by deleterious changes in oxidative phosphorylation, mitochondrial membrane potential, and ATP generation. As a consequence, ATP-dependent processes, like ion transport and protein synthesis, are disrupted [26]. Furthermore, the dysfunction of the respiratory chain in ischemia primes the mitochondria for excessive reactive oxygen species generation upon reperfusion, which further exacerbates tissue damage [27,28]. These alterations ultimately lead to cell death, often through necrosis rather than apoptosis, resulting in severe tissue damage. Although energetic stress represents a common challenge across tissues, the cellular responses to energy substrate deficiency are not uniform but are determined by tissue-specific metabolic features and adaptive mechanisms.

Astrocytes play a key role in neurometabolic coupling, supporting neurons by producing lactate and protecting them from oxidative stress [29,30]. Under ischemic conditions, energy deficit triggers a metabolic shift that preferentially affects astrocytes [30,31]. Due to their direct access to glucose from blood vessels, astrocytes increase glucose uptake and activate glycolysis, whereas these processes are less pronounced in neurons [32]. Furthermore, astrocytes demonstrate greater resilience, preserving mitochondrial function during ischemia [33]. Such compensatory mechanisms in the injured brain tissue, in particular after I/R, are consistent with a relative preservation of TCA and ETC expression profiles after I/R (Fig. 2a) [34,35].

Liver cells can flexibly utilize various metabolic substrates, such as fatty acids, glucose, amino acids, or ketone bodies, to fulfill their energy needs [7]. However, rapid replenishment of the ATP pool in liver cells relies on a stable ETC and healthy mitochondrial functions [36]. However, the observed transcriptional downregulation of genes encoding TCA cycle and ETC enzymes (Fig. 4) does not exclude the capacity of hepatocytes to partially compensate for energetic stress through alternative substrate utilization, a feature reflecting the hepatic ability to flexibly switch between energy substrates to compensate for the metabolic deficits. Such metabolic remodeling has consequences not only for hepatocyte energy balance but also for repairing tissue responses after injury. In the liver, these responses involve hepatic stellate cells playing a central role in remodeling processes and maintenance of hepatocyte function. These cells, at the same time, remain sensitive to metabolic and ischemic insults [37]. However, it is important to acknowledge that the use of the LX-2 cell line in isolation represents a limitation of this study. While liver stellate cells possess broad metabolic capabilities and contribute to hepatic metabolic plasticity, they do not fully replicate the metabolic landscape of the whole liver, where hepatocytes predominate.

In contrast to the liver, where metabolic flexibility may partially compensate for energetic stress, renal epithelial cells depend heavily on sustained mitochondrial oxidative metabolism to support energy-intensive functions essential for kidney homeostasis, including the reabsorption of glucose, electrolytes, and water, as well as the precise regulation of acid-base balance [38]. These processes demand substantial ATP production, making mitochondrial energetics critical for renal function. Under glucose deficiency, renal epithelial cells can shift toward fatty acid oxidation to replenish the pool of acetyl-CoA, because the oxidative phosphorylation remains central to their energy metabolism [39]. Consistent with this metabolic dependency, our transcriptome analysis reveals significant suppression of the gene expression of both mitochondrial respiratory chain complexes and TCA cycle enzymes in kidney tissue after I/R (Fig. 3). Compared to the liver and brain, this transcriptional response was more pronounced, indicating a high

vulnerability of the kidney to ischemic damage. Consistent with this interpretation, our analysis revealed increased Complex IV protein levels in astrocytes under deprivation conditions, while kidney epithelial cells showed increased GAPDH levels (Supplementary Fig. S4). Although these observations are limited to a small set of markers, they support the concept of organ-specific bioenergetic adaptation suggested by the transcriptomic data.

The deficiency of TCA cycle metabolites during ischemia poses a key challenge for the restoration of mitochondrial respiration, cellular metabolism, and normal organ function [40]. Our data underscore that metabolic flexibility, i.e., the ability to maintain energy homeostasis by remodeling major bioenergetic pathways, is not a universal property but rather a tissue-specific feature. Following injury, the inherent metabolic specialization of organs undergoes significant reorganization, which is reflected in substantial shifts in gene expression profiles (Fig. 1). This observation aligns with a number of previous studies describing injury-associated metabolic reprogramming in both acute injuries [41,42] and chronic pathologies [43–45]. Thus, while nervous tissue maintains or even upregulates the expression of TCA cycle and ETC genes in response to ischemia, kidney and liver tissues exhibit varying degrees of transcriptional repression of these pathways. Such transcriptomic patterns likely reflect fundamental differences in the organs' metabolic architecture rather than uniform sensitivity to energy substrate deficiency. This, in turn, may contribute to the differential vulnerability of various tissues to the availability of TCA cycle intermediates, such as fumarate.

The protective effect of fumarate-related compounds has been reported for a number of pathologies. Administration of sodium fumarate in the deoxycorticosterone acetate-salt hypertension model reduced the expression of the damage marker kidney injury molecule-1 (KIM-1) and restored kidney NO production [46]. In cellular models of hypoxia, it decreased cell death and partially restored the activity of ETC complex 1 [47]. In parallel, administration of bioavailable fumarate derivatives, particularly dimethyl fumarate and monomethyl fumarate, demonstrated cytoprotective effects in various pathologies. These effects have been largely attributed to activation of Nrf2-dependent antioxidant signaling pathways, resulting in reduced oxidative stress and improved cellular survival in models of kidney [48], hepatic [49], and brain injury [50–52]. Beyond mitigating oxidative stress, dimethyl fumarate has been reported to improve mitochondrial function in acute kidney injury, specifically by restoring succinate dehydrogenase activity [53]. There is growing evidence that fumarate itself can directly modulate the Nrf2 transcriptional pathway. For instance, sodium fumarate supplementation significantly restored the expression of Nrf2-associated antioxidant genes, including classical targets such as *Hmox1* and *Nqo1*, which had been suppressed in the model of metabolic stress [54]. The findings are supported by results from transgenic animals, in particular mice with knockout of fumarate hydratase, in which activation of Nrf2 signaling was also detected in the heart and kidneys [12,55].

In contrast to dimethyl fumarate and monomethyl fumarate, whose protective effects are largely attributed to well-characterized signaling pathways, the cellular actions of fumarate itself remain less clearly defined. Our data indicate that the organ-specific effects of fumarate are largely associated with mitochondrial function (Figs. 8–10). A limitation of this study is that we assessed only changes in mitochondrial membrane potential across different cell types in response to fumarate, without evaluating the corresponding changes in mitochondrial ultrastructural morphology. Nevertheless, fumarate accumulation can exacerbate organ damage [56,57]. Consistent with this, our data show that the highest concentration of fumarate (100 mM) induced cytotoxicity, most notably in kidney and liver cells under both normal and serum-deprived conditions (Fig. 7b,c,e,f). The use of disodium fumarate had a limitation inherent in the experimental design of our *in vitro* model regarding the physiological relevance of the millimolar fumarate concentrations employed. Fumarate derivatives are established therapeutic agents for hypoxic and critical

conditions, psoriasis and multiple sclerosis and are applied at lower concentrations due to their better permeability [58–60]. However, in this study it was important to exclude the hydrolysis products of methyl fumarate derivatives [61], so the disodium salt of fumaric acid was used.

The combined analysis of DAPI (Figs. 6 and 7) and MTT (Fig. S5) data revealed a tissue-specific dynamic of the response to fumarate. In astrocytes, both methods showed a consistent maximum protective effect under deprivation at 50 mM fumarate (Figs. 7a,d and S5a,d). In kidney epithelial cells, the MTT test revealed a significant increase in viability under deprivation at 50 mM fumarate (Fig. S5e), while no significant increase in nuclear counting was revealed (Fig. 7e). This may indicate a primary influence on metabolic activity rather than on the proliferation and restoration of kidney cells. In hepatic stellate cells, the data from both DAPI-staining and MTT methods correlate, demonstrating a shift in the optimum protective effect to a lower concentration range of 12.5–25 mM under both normal and stress conditions (Figs. 7c,f and S5c,f). Based on these findings, we propose that the tissue-specific action of fumarate may be attributed to its bioavailability, transport, or intracellular handling.

In health and disease, fumarate bioavailability is largely determined by the number of transporters and receptors with different affinities for this metabolite, as well as the activation of signaling cascades specific to each cell type. Pharmacodynamic analyses have demonstrated non-uniform tissue distribution of fumarate derivatives [62], suggesting the hypothesis of tissue-specific distribution of fumarate receptors, including hydroxyl carboxylic acid receptor-2 (HCAR2, also known as GPR109a). HCAR2 expression is significantly increased under inflammatory and hemolytic conditions, indicating its role in metabolic adaptation under stress [63]. In addition to its established role in lipid metabolism, HCAR2 participates in inflammatory response [64] through AMPK/SIRT1 signaling, which regulates microglia switching toward an anti-inflammatory and neuroprotective phenotype [65]. While direct involvement of this pathway was not examined in the present study, it is conceivable that high extracellular fumarate concentrations under deprivation conditions may engage similar signaling mechanisms in astrocytes, potentially contributing to the observed changes in cell number (Fig. 7d). Consistent with these results, the neuroprotective effect of fumarate and its derivatives has been demonstrated recently in cortical neuron cultures under oxygen-glucose deprivation [66] and in stroke models *in vivo* [51].

Beyond its metabolic role, fumarate can influence the epigenetic profile of cells by regulating the activity of Ten-Eleven Translocation DNA demethylases (TET) and Jumonji C domain-containing histone demethylases (JmjC). By competing with α-ketoglutarate, elevated fumarate levels inhibit many α-ketoglutarate-dependent demethylases, leading to changes in gene expression through changes in DNA and histone methylation patterns [67]. In our study, exposure to fumarate at concentrations ≥12.5 mM under deprivation conditions resulted in a decrease in the number of renal epithelial cells (Fig. 7e), which may be associated with the effect of fumarate on the epigenetic landscape of cells. It has been shown that under chronic metabolic stress, excess fumarate can impair the function of demethylases, promoting long-term changes in gene expression that affect inflammation and tissue repair [68].

Another possible mechanism regulating the tissue-specific action of fumarate involves fumarate hydratase 1 (FH1), which controls the accumulation of this metabolite in the cell. Genetic deficiency of FH1 leads to pathological fumarate accumulation and profound alterations in cellular signaling and epigenetic regulation, which result in the development of hereditary leiomyomatosis and renal cell carcinoma (HLRCC) [69]. While long-term deprivation does not affect FH1 expression, it significantly increases the expression of an alternative FH variant, which is associated with the cellular response to stress [70]. Thus, under deprivation conditions, fumarate can suppress renal epithelial proliferation by inactivating several demethylases and by inducing the FH variant, associated with cellular stress response. This may partially

explain the observed decrease in the number of renal epithelial cells after incubation with fumarate in stress conditions (Fig. 7e).

In addition to intracellular metabolism, an important role in the cell exposure to fumarate plays in the regulation of its transport. Fumarate is transported by the members of the solute carrier family (SLC), which are involved in transporting various TCA cycle intermediates. One of these transporters is SLC13A3, which is important for the transport of fumarate and other dicarboxylates in astrocytes, renal epithelial cells, and likely hepatic stellate cells [71–73]. Its dysfunction is associated with neurological and metabolic disorders, as well as the pathogenesis of liver diseases, making it a promising target for further research and therapy [71–73].

5 Conclusions

Replenishing TCA cycle intermediates, including fumarate, has been proposed as a promising strategy to support cellular metabolism during ischemic injury. Our data showed a tissue-specific effect of fumarate *in vitro* under both normal and pathological conditions. Under serum deprivation conditions, fumarate influenced mitochondrial status, as indicated by an increase in potential-dependent TMRE accumulation in astrocytes, renal epithelial cells, and hepatic stellate cells. However, a similar effect on mitochondria was accompanied by tissue-specific changes in cell number. These cell-specific, multidirectional effects of fumarate likely reflect distinct regulatory mechanisms, including differences in signaling pathways, epigenetic regulation, intracellular metabolism, and transport. Therefore, developing effective metabolite-based therapies for ischemic injury requires not only targeting energy imbalance but also accounting for the metabolic specialization and functional state of target cells.

Acknowledgement: We are grateful to the Moscow State University Development Program for providing access to the confocal microscope Zeiss LSM900 and CELENA® X High Content digital imaging system.

Funding Statement: This study was supported by the Russian Science Foundation (grant No. 24-75-10013), https://rscf.ru/project/24-75-10013/.

Author Contributions: The authors confirm contribution to the paper as follows: Conceptualization, Nadezda V. Andrianova, Egor Y. Plotnikov; methodology, Egor Y. Plotnikov, Marina I. Buyan, Nadezda V. Andrianova; validation, Marina I. Buyan, Kseniia S. Cherkesova; formal analysis, Kseniia S. Cherkesova, Andrey I. Buyan, Marina I. Buyan; investigation, Marina I. Buyan, Kseniia S. Cherkesova, Anna A. Brezgunova, Irina B. Pevzner, Nadezda V. Andrianova, Polina A. Abramicheva, Andrey I. Buyan; data curation, Kseniia S. Cherkesova, Marina I. Buyan, Andrey I. Buyan; writing—original draft preparation, Marina I. Buyan, Kseniia S. Cherkesova, Anna A. Brezgunova, Polina A. Abramicheva, Andrey I. Buyan; writing—review and editing, Nadezda V. Andrianova, Egor Y. Plotnikov, Irina B. Pevzner; visualization, Kseniia S. Cherkesova, Marina I. Buyan, Andrey I. Buyan; supervision, Nadezda V. Andrianova, Egor Y. Plotnikov; project administration, Nadezda V. Andrianova; funding acquisition, Nadezda V. Andrianova. All authors reviewed and approved the final version of the manuscript.

Availability of Data and Materials: The data supporting the findings of this study are available from the corresponding author, Egor Y. Plotnikov, upon reasonable request.

Ethics Approval: The animal study protocol was approved by the Ethics Committee of A. N. Belozersky Institute of Physico-Chemical Biology, Lomonosov Moscow State University (Protocol 019-4/07/2025).

Conflicts of Interest: The authors declare no conflicts of interest.

Supplementary Materials: The supplementary material is available online at https://www.techscience.com/doi/10.32604/biocell.2026.078925/s1.

Abbreviations

DAPI	4′,6-diamidino-2-phenylindole
ETC	Electron transport chain
I/R	Ischemia/reperfusion injury
TCA	Tricarboxylic acid cycle
TMRE	Tetramethylrhodamine ethyl ester

References

1. Li Q, Zhang S, Yang G, Wang X, Liu F, Li Y, et al. Energy metabolism: a critical target of cardiovascular injury. Biomed Pharmacother. 2023;165:115271. [CrossRef].
2. Preau S, Vodovar D, Jung B, Lancel S, Zafrani L, Flatres A, et al. Energetic dysfunction in sepsis: a narrative review. Ann Intensive Care. 2021;11(1):104. [CrossRef].
3. Eltzschig HK, Eckle T. Ischemia and reperfusion—from mechanism to translation. Nat Med. 2011;17(11):1391–401. [CrossRef].
4. Tzatsos A, Tsichlis PN. Energy depletion inhibits phosphatidylinositol 3-kinase/Akt signaling and induces apoptosis via AMP-activated protein kinase-dependent phosphorylation of IRS-1 at Ser-794. J Biol Chem. 2007;282(25):18069–82. [CrossRef].
5. Bonvento G, Bolaños JP. Astrocyte-neuron metabolic cooperation shapes brain activity. Cell Metab. 2021;33(8):1546–64. [CrossRef].
6. Gupta P, Zhu S, Gui Y, Zhou D. Metabolic chaos in kidney disease: unraveling energy dysregulation. J Clin Med. 2024;13(22):6772. [CrossRef].
7. Rui L. Energy metabolism in the liver. Compr Physiol. 2014;4(1):177–97. [CrossRef].
8. Solhi R, Lotfinia M, Gramignoli R, Najimi M, Vosough M. Metabolic hallmarks of liver regeneration. Trends Endocrinol Metab. 2021;32(9):731–45. [CrossRef].
9. Stowe DF. Mitochondrial function and bioenergetics. In: Evolution of Bioenergetics from Elements to Life. Cham, Switzerland: Springer Nature; 2025. p. 123–56. [CrossRef].
10. Bénit P, Letouzé E, Rak M, Aubry L, Burnichon N, Favier J, et al. Unsuspected task for an old team: succinate, fumarate and other Krebs cycle acids in metabolic remodeling. Biochim Biophys Acta. 2014;1837(8):1330–7. [CrossRef].
11. Edosuyi O, Igbe I, Oyekan A. Fumarate and its downstream signalling pathways in the cardiorenal system: recent insights and novel expositions in the etiology of hypertension. Eur J Pharmacol. 2023;961:176186. [CrossRef].
12. Ashrafian H, Czibik G, Bellahcene M, Aksentijević D, Smith AC, Mitchell SJ, et al. Fumarate is cardioprotective via activation of the Nrf2 antioxidant pathway. Cell Metab. 2012;15(3):361–71. [CrossRef].
13. Sánchez-García FJ, Pérez-Hernández CA, Rodríguez-Murillo M, Moreno-Altamirano MMB. The role of tricarboxylic acid cycle metabolites in viral infections. Front Cell Infect Microbiol. 2021;11:725043. [CrossRef].
14. Zhou G, Wang T, Zha XM. RNA-Seq analysis of knocking out the neuroprotective proton-sensitive GPR68 on basal and acute ischemia-induced transcriptome changes and signaling in mouse brain. FASEB J. 2021;35(4):e21461. [CrossRef].
15. Heruye SH, Myslinski J, Zeng C, Zollman A, Makino S, Nanamatsu A, et al. Inflammation primes the murine kidney for recovery by activating AZIN1 adenosine-to-inosine editing. J Clin Investig. 2024;134(17):e180117. [CrossRef].
16. Zabala V, Boylan JM, Thevenot P, Frank A, Senthoor D, Iyengar V, et al. Transcriptional changes during hepatic ischemia-reperfusion in the rat. PLoS One. 2019;14(12):e0227038. [CrossRef].
17. Kanehisa M, Furumichi M, Sato Y, Matsuura Y, Ishiguro-Watanabe M. KEGG: biological systems database as a model of the real world. Nucleic Acids Res. 2025;53(D1):D672–7. [CrossRef].
18. Castanza AS, Recla JM, Eby D, Thorvaldsdóttir H, Bult CJ, Mesirov JP. Extending support for mouse data in the Molecular Signatures Database (MSigDB). Nat Methods. 2023;20(11):1619–20. [CrossRef].

19. Varlamova EG, Baryshev AS, Gudkov SV, Babenko VA, Plotnikov EY, Turovsky EA. Cerium oxide nanoparticles protect cortical astrocytes from oxygen-glucose deprivation through activation of the Ca^{2+} signaling system. Int J Mol Sci. 2023;24(18):14305. [CrossRef].
20. Percie du Sert N, Hurst V, Ahluwalia A, Alam S, Avey MT, Baker M, et al. The ARRIVE guidelines 2.0: updated guidelines for reporting animal research. PLoS Biol. 2020;18(7):e3000410. [CrossRef].
21. Yu SB, Pekkurnaz G. Mechanisms orchestrating mitochondrial dynamics for energy homeostasis. J Mol Biol. 2018;430(21):3922–41. [CrossRef].
22. Midha AD, Zhou Y, Queliconi BB, Barrios AM, Haribowo AG, Chew BTL, et al. Organ-specific fuel rewiring in acute and chronic hypoxia redistributes glucose and fatty acid metabolism. Cell Metab. 2023;35(3):504–16.e5. [CrossRef].
23. Widgerow AD. Ischemia-reperfusion injury: influencing the microcirculatory and cellular environment. Ann Plast Surg. 2014;72(2):253–60. [CrossRef].
24. Dorweiler B, Pruefer D, Andrasi TB, Maksan SM, Schmiedt W, Neufang A, et al. Ischemia-reperfusion injury: pathophysiology and clinical implications. Eur J Trauma Emerg Surg. 2007;33(6):600–12. [CrossRef].
25. Lippi G, Favaloro EJ, Cervellin G. Massive posttraumatic bleeding: epidemiology, causes, clinical features, and therapeutic management. Semin Thromb Hemost. 2013;39(1):83–93. [CrossRef].
26. Goncharov RG, Sharapov MG. Ischemia-reperfusion injury: molecular mechanisms of pathogenesis and methods of their correction. Mol Biol. 2023;57(6):1150–74. [CrossRef].
27. Chen Q, Moghaddas S, Hoppel CL, Lesnefsky EJ. Ischemic defects in the electron transport chain increase the production of reactive oxygen species from isolated rat heart mitochondria. Am J Physiol Cell Physiol. 2008;294(2):C460–6. [CrossRef].
28. Bhatti JS, Bhatti GK, Reddy PH. Mitochondrial dysfunction and oxidative stress in metabolic disorders—A step towards mitochondria based therapeutic strategies. Biochim Biophys Acta Mol Basis Dis. 2017;1863(5):1066–77. [CrossRef].
29. Joseph UG, Oyovwi MO, Jeroh E, Esuku DT, Ben-Azu B. Dysfunctional astrocyte metabolism: a driver of imbalanced excitatory/inhibitory tone and support for therapeutic intervention targets. J Mol Pathol. 2025;6(2):12. [CrossRef].
30. Zhang YM, Qi YB, Gao YN, Chen WG, Zhou T, Zang Y, et al. Astrocyte metabolism and signaling pathways in the CNS. Front Neurosci. 2023;17:1217451. [CrossRef].
31. Deitmer JW, Theparambil SM, Ruminot I, Noor SI, Becker HM. Energy dynamics in the brain: contributions of astrocytes to metabolism and pH homeostasis. Front Neurosci. 2019;13:1301. [CrossRef].
32. Takahashi S. Neuroprotective function of high glycolytic activity in astrocytes: common roles in stroke and neurodegenerative diseases. Int J Mol Sci. 2021;22(12):6568. [CrossRef].
33. Gürer G, Gursoy-Ozdemir Y, Erdemli E, Can A, Dalkara T. Astrocytes are more resistant to focal cerebral ischemia than neurons and die by a delayed necrosis. Brain Pathol. 2009;19(4):630–41. [CrossRef].
34. Wei Z, Wu R, Zhang L, Xu P. ATPIF1 alleviates oxygen glucose deprivation/reoxygenation-induced astrocyte injury *in vitro*: a rat model of ischemic brain injury. Adv Clin Exp Med. 2023;32(7):791–802. [CrossRef].
35. Kim MJ, Hur J, Ham IH, Yang HJ, Kim Y, Park S, et al. Expression and activity of the na-k ATPase in ischemic injury of primary cultured astrocytes. Korean J Physiol Pharmacol. 2013;17(4):275–81. [CrossRef].
36. Shi S, Wang L, van der Laan LJW, Pan Q, Verstegen MMA. Mitochondrial dysfunction and oxidative stress in liver transplantation and underlying diseases: new insights and therapeutics. Transplantation. 2021;105(11):2362–73. [CrossRef].
37. Bansal MB. Hepatic stellate cells: fibrogenic, regenerative or both? Heterogeneity and context are key. Hepatol Int. 2016;10(6):902–8. [CrossRef].
38. Clark AJ, Parikh SM. Mitochondrial metabolism in acute kidney injury. Semin Nephrol. 2020;40(2):101–13. [CrossRef].
39. Wang T, Huang Y, Zhang X, Zhang Y, Zhang X. Advances in metabolic reprogramming of renal tubular epithelial cells in sepsis-associated acute kidney injury. Front Physiol. 2024;15:1329644. [CrossRef].
40. Andrianova NV, Buyan MI, Brezgunova AA, Cherkesova KS, Zorov DB, Plotnikov EY. Hemorrhagic shock and mitochondria: pathophysiology and therapeutic approaches. Int J Mol Sci. 2025;26(5):1843. [CrossRef].

41. He S, He L, Yan F, Li J, Liao X, Ling M, et al. Identification of hub genes associated with acute kidney injury induced by renal ischemia-reperfusion injury in mice. Front Physiol. 2022;13:951855. [CrossRef].
42. Kingsmore KM, Bachali P, Catalina MD, Daamen AR, Heuer SE, Robl RD, et al. Altered expression of genes controlling metabolism characterizes the tissue response to immune injury in lupus. Sci Rep. 2021;11(1):14789. [CrossRef].
43. Bhadra S, Chen S, Liu C. Analysis of differentially expressed genes that aggravate metabolic diseases in depression. Life. 2021;11(11):1203. [CrossRef].
44. Middleton FA, Mirnics K, Pierri JN, Lewis DA, Levitt P. Gene expression profiling reveals alterations of specific metabolic pathways in schizophrenia. J Neurosci. 2002;22(7):2718–29. [CrossRef].
45. Das MK, Savidge B, Pearl JE, Yates T, Miles G, Pareek M, et al. Altered hepatic metabolic landscape and insulin sensitivity in response to pulmonary tuberculosis. PLoS Pathog. 2024;20(9):e1012565. [CrossRef].
46. Edosuyi O, Choi M, Igbe I, Oyekan A. Fumarate exerted an antihypertensive effect and reduced kidney injury molecule (KIM)-1 expression in deoxycorticosterone acetate-salt hypertension. Clin Exp Hypertens. 2021;43(6):555–64. [CrossRef].
47. Vinokurov AY, Popov SV, Belyakov DY, Popov DY, Nikulin AS, Zakrzhevskaya VD, et al. Cytoprotective action of sodium fumarate in an *in vitro* model of hypoxia using sodium dithionite. Sovrem Tekhnologii Med. 2025;17(1):93–106. [CrossRef].
48. Yang Y, Cai F, Zhou N, Liu S, Wang P, Zhang S, et al. Dimethyl fumarate prevents ferroptosis to attenuate acute kidney injury by acting on NRF2. Clin Transl Med. 2021;11(4):e382. [CrossRef].
49. Qi D, Chen P, Bao H, Zhang L, Sun K, Song S, et al. Dimethyl fumarate protects against hepatic ischemia-reperfusion injury by alleviating ferroptosis via the NRF2/SLC7A11/HO-1 axis. Cell Cycle. 2023;22(7):818–28. [CrossRef].
50. Yao Y, Miao W, Liu Z, Han W, Shi K, Shen Y, et al. Dimethyl fumarate and monomethyl fumarate promote post-ischemic recovery in mice. Transl Stroke Res. 2016;7(6):535–47. [CrossRef].
51. Clausen BH, Lundberg L, Yli-Karjanmaa M, Martin NA, Svensson M, Alfsen MZ, et al. Fumarate decreases edema volume and improves functional outcome after experimental stroke. Exp Neurol. 2017;295:144–54. [CrossRef].
52. Zhao X, Sun G, Zhang J, Ting SM, Gonzales N, Aronowski J. Dimethyl fumarate protects brain from damage produced by intracerebral hemorrhage by mechanism involving Nrf2. Stroke. 2015;46(7):1923–8. [CrossRef].
53. Ashari S, Naghsh N, Salari Y, Barghi NG, Bagheri A. Dimethyl fumarate attenuates di-(2-ethylhexyl) phthalate-induced nephrotoxicity through the Nrf2/HO-1 and NF-κB signaling pathways. Inflammation. 2023;46(1):453–67. [CrossRef].
54. Meng M, Zhao X, Huo R, Li X, Chang G, Shen X. Disodium fumarate alleviates endoplasmic reticulum stress, mitochondrial damage, and oxidative stress induced by the high-concentrate diet in the mammary gland tissue of hu sheep. Antioxidants. 2023;12(2):223. [CrossRef].
55. Adam J, Hatipoglu E, O'Flaherty L, Ternette N, Sahgal N, Lockstone H, et al. Renal cyst formation in Fh1-deficient mice is independent of the Hif/Phd pathway: roles for fumarate in KEAP1 succination and Nrf2 signaling. Cancer Cell. 2011;20(4):524–37. [CrossRef].
56. Li ZL, Huang MM, Yu MY, Nie DF, Fu SL, Di JJ, et al. Mitochondrial fumarate promotes ischemia/reperfusion-induced tubular injury. Acta Physiol. 2024;240(4):e14121. [CrossRef].
57. Wentzel JF, Lewies A, Bronkhorst AJ, van Dyk E, du Plessis LH, Pretorius PJ. Exposure to high levels of fumarate and succinate leads to apoptotic cytotoxicity and altered global DNA methylation profiles *in vitro*. Biochimie. 2017;135:28–34. [CrossRef].
58. Hoogendoorn A, Avery TD, Li J, Bursill C, Abell A, Grace PM. Emerging therapeutic applications for fumarates. Trends Pharmacol Sci. 2021;42(4):239–54. [CrossRef].
59. Narapureddy B, Dubey D. Clinical evaluation of dimethyl fumarate for the treatment of relapsing-remitting multiple sclerosis: efficacy, safety, patient experience and adherence. Patient Prefer Adherence. 2019;13:1655–66. [CrossRef].
60. Kusnirikova ZK, Kacirova I, Pesakova V, Hradilek P, Brozmanova H, Grundmann M. Analysis of concentrations of monomethyl fumarate in patients with multiple sclerosis: result from routine health care. CNS Neurol Disord Drug Targets. 2024;23(12):1516–23. [CrossRef].

61. Kopincova J, Bernatova I. Dimethyl fumarate vs. monomethyl fumarate: unresolved pharmacologic issues. Pharmaceutics. 2025;17(12):1506. [CrossRef].
62. Brennan MS, Patel H, Allaire N, Thai A, Cullen P, Ryan S, et al. Pharmacodynamics of dimethyl fumarate are tissue specific and involve NRF2-dependent and-independent mechanisms. Antioxid Redox Signal. 2016;24(18):1058–71. [CrossRef].
63. Grunenwald A, Peliconi J, Zarantonello A, Dimitrov JD, Roumenina LT, Merle NS. HCAR2 is a novel receptor for heme. Blood Adv. 2025;9(17):4458–69. [CrossRef].
64. Testai L, Guida F, Salerno S, Brogi S, Morace AM, Carbonetti L, et al. Hydroxyl carboxylic acid receptor-2 (HCAR2) as a potential target in neurometabolic diseases. Pharmacol Ther. 2025;274:108909. [CrossRef].
65. Parodi B, Rossi S, Morando S, Cordano C, Bragoni A, Motta C, et al. Fumarates modulate microglia activation through a novel HCAR2 signaling pathway and rescue synaptic dysregulation in inflamed CNS. Acta Neuropathol. 2015;130(2):279–95. [CrossRef].
66. Lin R, Cai J, Kostuk EW, Rosenwasser R, Iacovitti L. Fumarate modulates the immune/inflammatory response and rescues nerve cells and neurological function after stroke in rats. J Neuroinflammation. 2016;13(1):269. [CrossRef].
67. Xiao M, Yang H, Xu W, Ma S, Lin H, Zhu H, et al. Inhibition of α-KG-dependent histone and DNA demethylases by fumarate and succinate that are accumulated in mutations of FH and SDH tumor suppressors. Genes Dev. 2012;26(12):1326–38. [CrossRef].
68. Zheng XL, Yin H. Fumarate signaling in cardiovascular disease: therapeutic potential and pathologic pitfalls of DMF/MMF and FH1 deficiency. J Cardiovasc Transl Res. 2025;18(5):1283–97. [CrossRef].
69. D'Indinosante M, Lardino S, Bruno M, Stabile G, Pavone M, Giannone G, et al. Implications of fumarate hydratase deficiency (FHD) and cancer risk: a window into the clinical and oncological implications of a rare disorder in gynecology. Cancers. 2025;17(4):573. [CrossRef].
70. Lehtonen HJ, Ylisaukko-Oja SK, Kiuru M, Karhu A, Lehtonen R, Vanharanta S, et al. Stress-induced expression of a novel variant of human fumarate hydratase (FH). Gene Expr. 2007;14(2):59–69. [CrossRef].
71. Dewulf JP, Wiame E, Dorboz I, Elmaleh-Bergès M, Imbard A, Dumitriu D, et al. SLC13A3 variants cause acute reversible leukoencephalopathy and α-ketoglutarate accumulation. Ann Neurol. 2019;85(3):385–95. [CrossRef].
72. Bergeron MJ, Clémençon B, Hediger MA, Markovich D. SLC13 family of Na^+-coupled di- and tri-carboxylate/sulfate transporters. Mol Aspects Med. 2013;34(2–3):299–312. [CrossRef].
73. Zhao W, Wang X, Han L, Zhang C, Wang C, Kong D, et al. SLC13A3 is a major effector downstream of activated β-catenin in liver cancer pathogenesis. Nat Commun. 2024;15(1):7522. [CrossRef].